中国激光

基于熔池图像不变矩特征的激光-MIG复合焊接根部驼峰在线检测方法

黄宇辉，范西岸，张艳喜，高向东*

广东工业大学广东省焊接工程技术研究中心，广东 广州 510006

摘要 根部驼峰缺陷是激光-MIG复合焊接(MIG焊，熔化极惰性气体保护焊)中常出现的焊接缺陷之一，因该缺陷出现在焊件背部，所以在焊接过程中不易被发现。为检测根部驼峰缺陷，采用高速摄像机捕捉焊接图像。对预处理后的图像进行阈值分割得到熔池轮廓图像，通过局部形态学处理进一步获取熔池二值化图像。提取二值化图像的四组归一化不变矩，并采用滑动均值法进行降噪处理，进而获得不变矩特征。建立动态调整学习率算法的一维卷积神经网络模型，以熔池尾部图像的四组归一化不变矩及其滑动均值作为输入。通过9150个连续焊缝样本检测值和实际值的比较，验证了该网络模型具有良好的检测能力。该方法可应用于封闭式的平板对接焊，通过采集激光-MIG复合焊接中焊件表面信号，对无法直接观察的背部驼峰缺陷进行检测。

关键词 激光技术；神经网络；激光-MIG复合焊；根部驼峰；熔池图像；图像不变矩

中图分类号 TG409 **文献标志码** A **DOI**：10.3788/CJL220922

1 引 言

激光-MIG复合焊接(MIG焊，熔化极惰性气体保护焊)既兼具激光焊接高功率密度、大深宽比等优势[1]，又保留了电弧焊良好的桥接性能[2]。激光的加入可以使电弧和熔滴过渡更稳定，同时电弧可以提高焊件对激光的吸收率。在激光-MIG复合焊接过程中，焊缝成形与复合焊接过程中熔滴过渡的形式密切相关[3]，激光与电弧两种热源相互耦合对焊接质量产生至关重要的影响[4]。在焊接熔透效率不足时，焊缝容易出现根部驼峰缺陷[5]。导致根部驼峰出现的因素主要包括熔融金属表面张力与重力的相互作用[6]、匙孔熔透状态[7]、背部焊缝几何形状[8]以及向下流动至匙孔出口的熔融金属速度[9]等。出现根部驼峰缺陷的背部熔融金属温度往往高于上表面，高温引起的表面张力减小，使底部过热的熔融金属无法向上流回内部熔池，最终在背部熔池末端凝固形成根部驼峰[10]。根部驼峰缺陷是由一段时间内流至焊缝背部熔池末端的熔融金属累积而成，当熔融金属凝固形成驼峰后，新的熔融金属又会在下一个位置继续堆积形成新的驼峰，导致该缺陷在一定范围内周期性出现[11]。

视觉检测技术被广泛应用在焊接过程中，其采集的图像含有丰富的焊接信息[12-15]。Fan等[16]采用双高速摄像系统，实时获取激光-MIG复合焊接过程中匙孔和熔池的图像。利用所提取的匙孔形态特征，可区分根部驼峰缺陷和正常熔透状态。但该方法需要采集较大数量的匙孔质心数据进行波动分析，实现在线检测较为困难。Gao等[17]利用高速摄像机分析焊接过程中熔池阴影的变化，从图像中提取阴影的面积、质心、最大宽度和阴影到匙孔的距离四个参数，实现焊接质量的在线检测。但是面积、质心等简单的形态特征无法区分一些特殊图像形态，不适用于描述复杂图像形态特征。Fan等[18]采用高速摄像机提取焊件顶部和底部的图像形态特征，通过经验模态分析特征的时序并构建支持向量机模型，检测焊缝是否存在根部驼峰等缺陷。该方法需要采集熔池背部的图像，不适用于无法获取背部图像信息的封闭式焊接场合。

焊缝根部驼峰直接影响着焊接质量，当前国内外关于焊缝根部驼峰的在线检测研究相对较少。因此，本文提出一种在激光-MIG复合焊接强噪声环境下，采集焊件表面复杂形态特征在线检测焊接过程中焊件背部根部驼峰缺陷的方法。熔池图像由高速摄像机采集，采用基于视网膜大脑皮层(Retinex)理论的多尺度视网膜大脑皮层(MSR)增强图像的熔池形貌，通过阈值分割和形态学处理提取出熔池尾部的二值化图像。计算图像的四组归一化不变矩，并采用滑动均值法减少噪声对不变矩的影响。同时，构建基于一维卷积神经网络的根部驼峰检测模型，实现根部驼峰缺陷的在线检测。

收稿日期：2022-05-30；**修回日期**：2022-09-21；**录用日期**：2022-11-04；**网络首发日期**：2022-11-14

基金项目：广州市科技计划(202002020068)、国家自然科学基金(52275317)、广东省自然科学基金项目(2314050004977)

通信作者：*gaoxd666@126.com

2　激光-MIG 复合焊接试验

2.1　激光-MIG 复合焊接过程中的检测试验装置

激光-MIG 复合焊接试验平台由光纤激光器、六轴机器人、高速摄像机等组成，如图 1 所示。光纤激光器的最大输出功率为 4 kW，高速摄像机采集的图像像素为 768 pixel×768 pixel，采集帧率为 2000 frame/s，搭配窄带近红外滤光系统，提取熔池和匙孔信息。高速摄像机镜头距离焊缝约 600 mm，与水平方向成 45°夹角。焊件尺寸是 200 mm×100 mm×3 mm，母材为 304 不锈钢，焊丝材质为 ER308 不锈钢。焊接采用电弧引导的形式，MIG 焊枪在前，激光在后。高速摄像机、激光头和电弧焊枪被固定，运动平台带动工件运动。

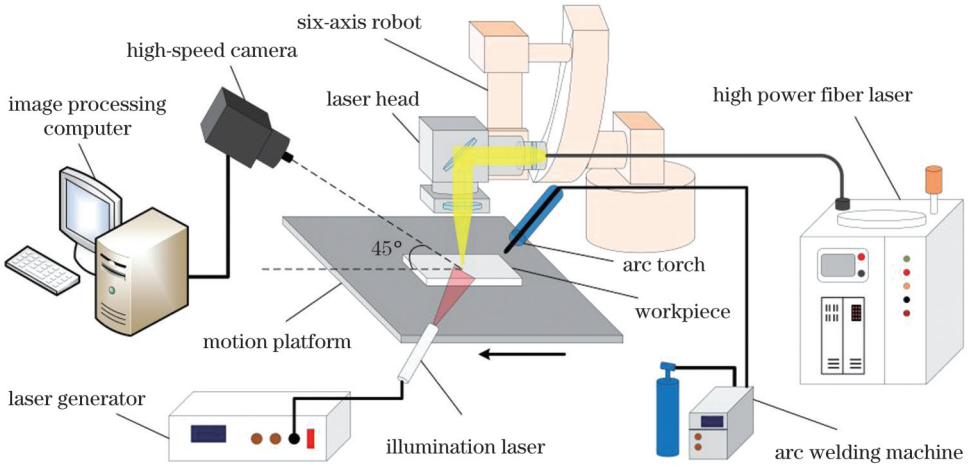

图 1　激光-MIG 复合焊接试验平台示意图

Fig. 1　Schematic of laser-MIG hybrid welding testing platform

2.2　焊接试验中的熔池变化

焊缝的成形与熔池的流动密切相关[19-20]，当出现根部驼峰缺陷时，焊件表面的部分熔池将转移到焊件背部，使得焊件表面熔池余高降低，并在背部累积形成根部驼峰[21]。如图 2(a)所示，当出现根部驼峰缺陷时，熔池表面两侧的凝固速度较快，熔池尾部两侧出现较大面积的灰色凝固区域。在熔宽变化不大的情况下，余高较小的熔池的表面曲率较小，近似于平面，从相机位置观察，凝固与未凝固区域的分界线趋近于斜线，熔池尾部呈“V”形。如图 2(b)所示，当全熔透时，焊接过程中熔池表面曲率更大，从相机位置观察，凝固与未凝固区域的分界线受表面熔池曲率的影响而弯曲，分界线形状为曲线，熔池尾部呈“U”形。

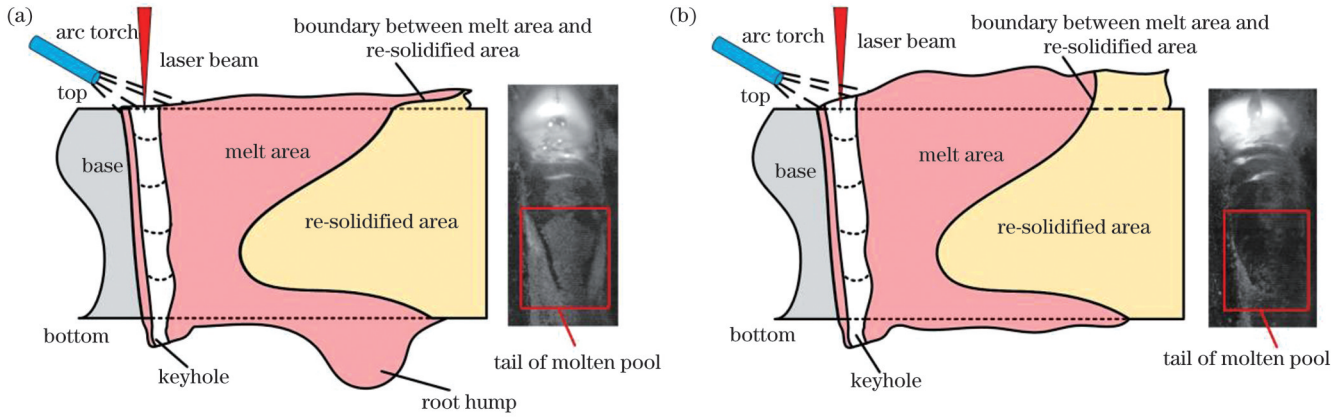

图 2　激光-MIG 复合焊接熔池示意图。(a)根部驼峰熔池形成过程；(b)全熔透缺陷熔池形成过程

Fig. 2　Schematics of laser-MIG hybrid welding molten pool. (a) Formation process of root hump pool; (b) formation process of full penetration defect pool

3　熔池不变矩特征的提取与分析

3.1　熔池尾部图像处理

图 3 为焊接过程中的检测图像，合适的图像处理算法可以提取图像潜藏的特征信息[22]，其中 ROI 表示感兴趣区域。由于在激光-MIG 复合焊接试验中，辅助激光从焊缝旁边进行照明，高速摄像机拍摄的原始图像左边的灰度高于右边，同时激光与电弧耦合区域的灰度也高于熔池尾部区域，如图 4(a)所示。为了完整提取熔池尾部的图像特征，采用基于 Retinex 理论的 MSR 增强

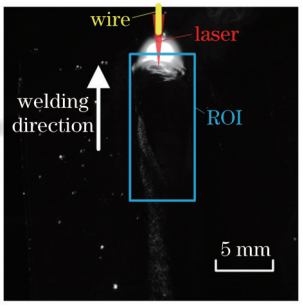

图 3　激光-MIG 复合焊接过程中的检测图像

Fig. 3　Detection image in laser-MIG hybrid welding process

对 ROI 进行预处理，MSR 增强利用原始图像估计光照分量，再去除或降低光照分量，获得物体的反射性质，从而抑制光照不均对物体原貌产生的影响[23-24]。熔池预处理图像如图 4(b)所示。在熔池尾部区域使用最大类间方差法(OTSU)对预处理图像进行阈值分割，通过局部形态学处理消除熔池和基材反光的影响，提取出熔池尾部灰色凝固区域的二值图像，熔池凝固区域的二值图像如图 4(c)所示。设置图像中的熔池尾部感兴趣区域，在该区域对图像进行黑白取反，得到表征熔池尾部形态的二值图像，熔池尾部的二值图像如图 4(d)所示。

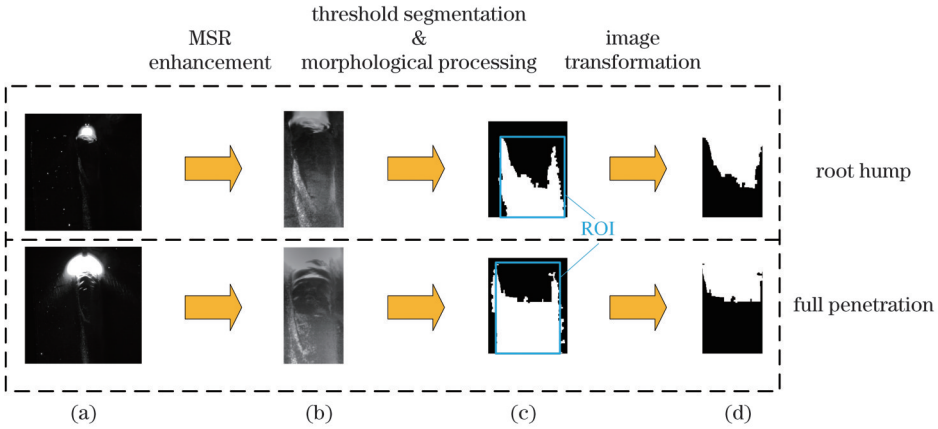

图 4　激光-MIG 复合焊接熔池的图像处理过程。(a)原始图像；(b)经过 MSR 处理后的熔池图像；(c)凝固熔池图像；(d)熔池尾部图像

Fig. 4　Image processing of laser-MIG hybrid welding molten pool. (a) Original image; (b) molten pool image after MSR processing; (c) image of solidified molten pool; (d) image of molten pool tail

3.2　熔池尾部图像的特征提取

图像不变矩是一种具有平移、旋转和尺度不变性的图像特征，用于对图像特征的描述[25]。利用图像的不变矩特征可以量化有根部驼峰缺陷的熔池尾部图像与全熔透的熔池尾部图像的差异。

熔池尾部二维图像 $f(x,y)$ 的 $p+q$ 阶矩[26]定义为

$$M_{pq}=\sum_{x=0}^{X-1}\sum_{y=0}^{Y-1}x^p y^q f(x,y), \tag{1}$$

式中：p 和 q 为阶数，取值 0，1，2，…；X 为图像的宽度；Y 为图像的高度；x 为图像的横坐标；y 为图像的纵坐标；$f(x,y)$ 为该坐标下图像的像素取值，取值为 0 或者 1。

因此，熔池尾部二维图像 $f(x,y)$ 的 $p+q$ 阶中心矩定义为

$$\mu_{pq}=\sum_{x=0}^{X-1}\sum_{y=0}^{Y-1}f(x,y)(x-\bar{x})^p(y-\bar{y})^q, \tag{2}$$

式中：$\bar{x}$ 为熔池尾部图像白色区域质心的横坐标，其值为 M_{10}/M_{00}；$\bar{y}$ 为熔池尾部图像白色区域质心的纵坐标，其值为 M_{01}/M_{00}。

熔池尾部二维图像 $f(x,y)$ 的 $p+q$ 阶归一化中心矩定义为

$$\begin{cases}\eta_{pq}=\dfrac{\mu_{pq}}{\mu_{00}^{\gamma}}\\ \gamma=\dfrac{p+q}{2}+1,\ p+q=2,3,\cdots\end{cases}。 \tag{3}$$

式(2)的中心矩具有平移不变性，式(3)的归一化中心矩具有比例不变性，在此基础上由不高于三阶的归一化中心矩构造出四组不变矩[27]：

$$\begin{cases}\varphi_1=\eta_{20}+\eta_{02}\\ \varphi_2=(\eta_{20}-\eta_{02})^2+4\eta_{11}^2\\ \varphi_3=(\eta_{30}-3\eta_{12})^2+(3\eta_{21}-\eta_{03})^2\\ \varphi_4=(\eta_{30}+\eta_{12})^2+(\eta_{21}+\eta_{03})^2\end{cases}。 \tag{4}$$

通过式(4)分别计算两种焊接状态图像的四组不变矩，并将每组不变矩数据进行归一化处理，消除特征的量纲影响。第 i 组 t 时刻的归一化不变矩定义为

$$\varphi_{i\,\mathrm{norm}}(t)=\frac{\varphi_i(t)-\varphi_{i\min}}{\varphi_{i\max}-\varphi_{i\min}}, \tag{5}$$

式中：i 为不变矩类型编号；$\varphi_i(t)$ 为 t 时刻第 i 组不变矩的值；$\varphi_{i\min}$ 为 $\varphi_i(t)$ 的最小值；$\varphi_{i\max}$ 为 $\varphi_i(t)$ 的最大值。

采用滑动均值法处理每组归一化后的不变矩数据，从而平滑数据，消除随机误差产生的局部噪点，突显每组归一化后的不变矩变化趋势。第 i 组 t 时刻的归一化不变矩滑动均值定义为

$$\bar{\varphi}_i(t)=\frac{1}{w}\sum_{t=n-w+1}^{n}\varphi_{i\,\mathrm{norm}}(t), \tag{6}$$

式中：w 为滑动窗口宽度；n 为样本总数。

3.3　熔池尾部特征的序列分析

选取有根部驼峰缺陷和全熔透的连续焊接样本各12000个，两种焊接状态的四组归一化不变矩及其滑动均值如图5所示。图5(a)为两种样本的φ_{1norm}，全熔透样本的φ_{1norm}为0.080，方差为0.010；而有缺陷样本的φ_{1norm}为0.197，方差为0.012。在对应的箱线图中全熔透的中位数比有缺陷的低0.13，其上下限范围也比有缺陷的小0.21，如图6(a)所示。图5(b)为两种样本的φ_{2norm}，全熔透样本的φ_{2norm}为0.083，方差为0.018；而有缺陷样本的φ_{2norm}为0.317，方差为0.025。在对应的箱线图中全熔透的中位数比有缺陷的低0.26，其上下限范围也比有缺陷的小0.50，如图6(b)所示。图5(c)为两种样本的φ_{3norm}，全熔透样本的φ_{3norm}均值为0.097，方差为0.018；而有缺陷样本的φ_{3norm}为0.189，方差为

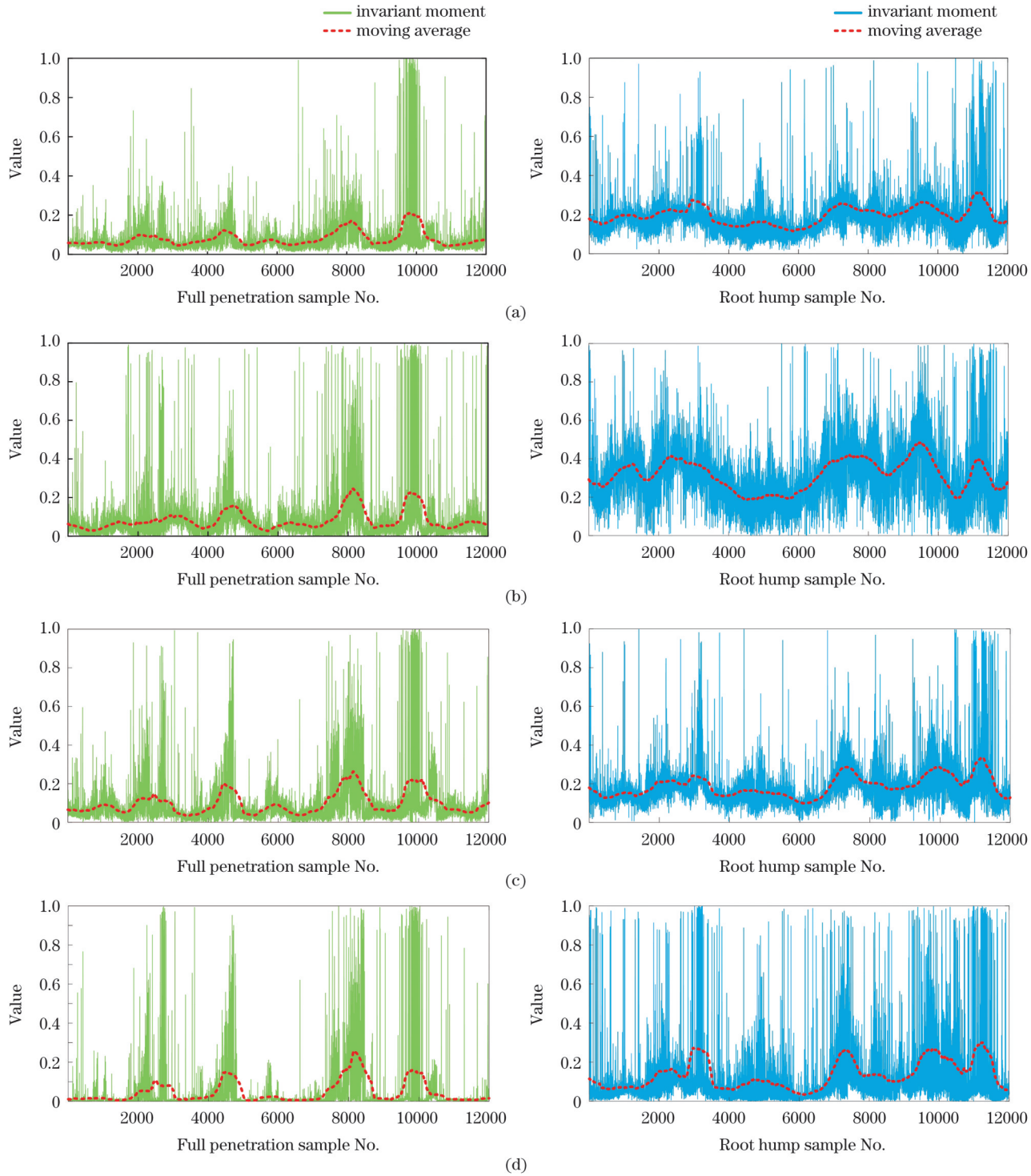

图5　熔池尾部图像的不变矩及其滑动均值。(a)不变矩1；(b)不变矩2；(c)不变矩3；(d)不变矩4

Fig. 5　Invariant moments and moving average values of molten pool tail images. (a) Invariant moment 1; (b) invariant moment 2; (c) invariant moment 3; (d) invariant moment 4

0.014。在对应的箱线图中全熔透的中位数比有缺陷的低0.11，其上下限范围也比有缺陷的小0.18，如图6(c)所示。图5(d)为两种样本的$\varphi_{4\mathrm{norm}}$，全熔透样本的$\varphi_{4\mathrm{norm}}$为0.048，方差为0.021；而有缺陷样本的$\varphi_{4\mathrm{norm}}$为0.135，方差为0.034。在对应的箱线图中全熔透的中位数比有缺陷的低0.07，其上下限范围也比有缺陷的小0.28，如图6(d)所示。有根部驼峰缺陷的下四分位数均高于全熔透的上四分位数，两者的四组归一化不变矩四分位间距框之间没有重叠部分，有根部驼峰缺陷的样本的特征值也比全熔透更分散。有根部驼峰缺陷的四组归一化不变矩均值相比于全熔透至少增加了90%，而其中位数相比于全熔透至少增加了150%。

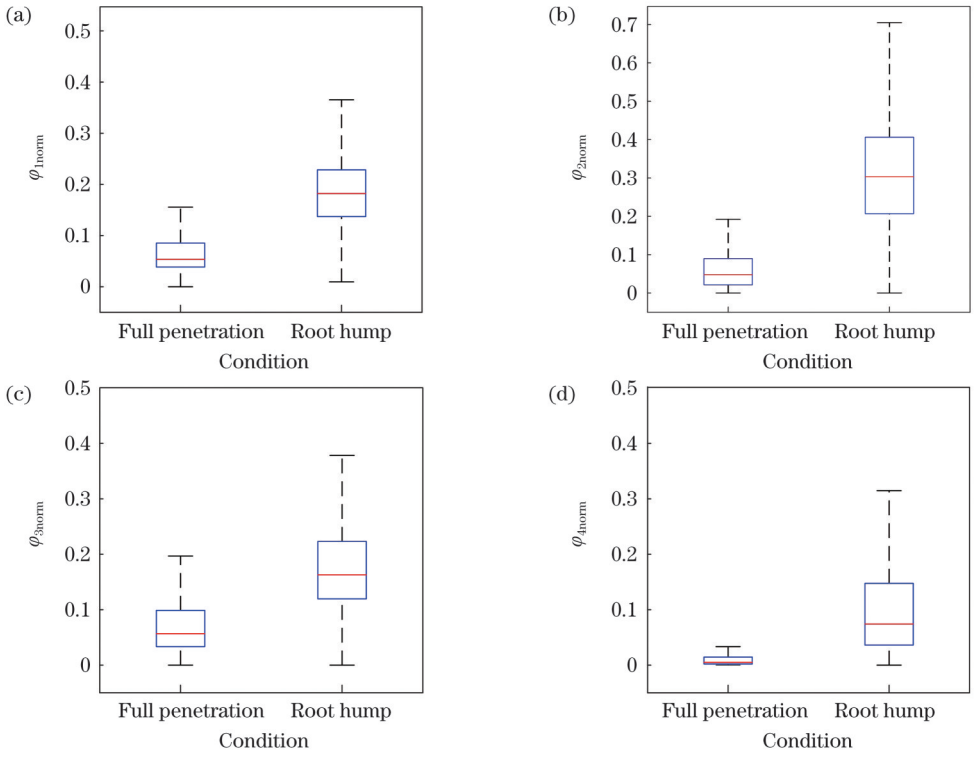

图6 熔池尾部图像不变矩的箱线图。(a)不变矩1；(b)不变矩2；(c)不变矩3；(d)不变矩4

Fig. 6 Boxplots of invariant moment of molten pool tail image. (a) Invariant moment 1; (b) invariant moment 2; (c) invariant moment 3; (d) invariant moment 4

4 焊缝缺陷检测模型

4.1 一维卷积神经网络模型的建立

卷积神经网络是当前人工智能领域最具代表性的深度学习算法之一，其中一维卷积神经网络适用于处理一维时间序列数据[28-29]。为检测激光-MIG复合焊接过程中是否出现根部驼峰缺陷，建立了一维卷积神经网络模型，模型前四组为卷积层(Conv)和池化层(pooling)，最后一组为一个池化层和一个全连接层，一维卷积神经网络模型如图7所示。本次试验采集的有根部驼峰缺陷和全熔透的样本各12000份，以四组归一化不变矩及其滑动均值作为输入量即$X_t=\{\bar{\varphi}_1(t), \varphi_{1\mathrm{norm}}(t), \bar{\varphi}_2(t), \varphi_{2\mathrm{norm}}(t), \bar{\varphi}_3(t), \varphi_{3\mathrm{norm}}(t), \bar{\varphi}_4(t), \varphi_{4\mathrm{norm}}(t), t=0.5, 1.0, 1.5, \cdots, 12000\ \mathrm{ms}\}$，输出量为$Y_t$，对焊缝成型状况进行分类。若$Y_t$为0，表示样本为全熔透状态；若$Y_t$为1，表示样本含有驼峰缺陷。一维卷积神经网络模型的训练次数(epoch)为30，每批次学习的样本数量(batch size)为128，初始学习率(learning rate)为0.01。本次试验采用的学习率动态调整算法，由验证集准确率进行调控。学习率不进行调整的容忍轮数设置为5轮，即经过5轮训练后，若验证集的准确率没有提升，则对学习率进行调整，调整因子为0.2。

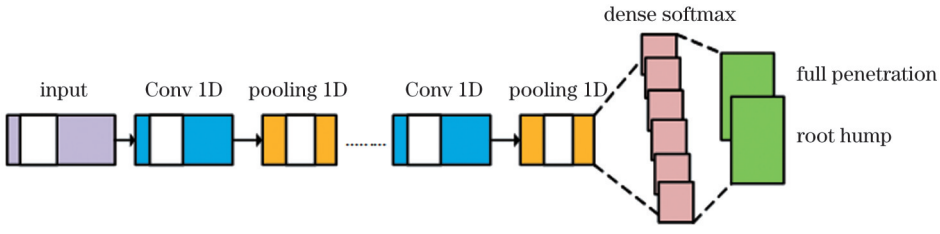

图7 用于焊缝根部驼峰检测的一维卷积神经网络模型

Fig. 7 One-dimensional convolutional neural network model for weld root hump detection

4.2　模型训练结果

根部驼峰缺陷的一维卷积神经网络检测模型的准确率曲线如图 8(a)所示。模型的训练集和验证集准确率分别在第 21 轮和第 22 轮训练时达到峰值，模型训练集和验证集最佳准确率分别为 99.73% 和 99.88%。模型的损失值曲线如图 8(b)所示，模型的损失值曲线在 20 轮左右开始收敛，并且模型的损失值最终趋近于 1%。模型的学习率曲线如图 8(c)所示，模型的学习率先降低到 2×10^{-5}，再进一步降低到 4×10^{-6}。初始学习率持续了 25 轮，一个学习率参数持续的轮次越多，证明该模型在该学习率参数下能学到的特征越多，性能提升的空间越大。学习率动态调整算法成功避免了预测模型的多次提前收敛，从而得到了性能最佳的缺陷检测模型。

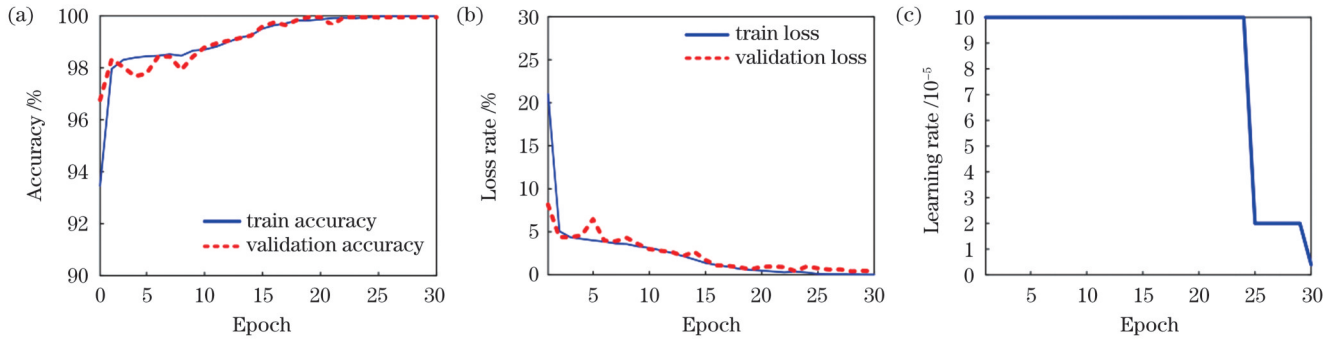

图 8　用于焊缝根部驼峰检测的一维卷积神经网络模型的训练结果。(a)模型准确率曲线；(b)模型损失值曲线；(c)模型学习率曲线

Fig. 8　Training results of one-dimensional convolutional neural network model for weld root hump detection. (a) Accuracy curves of model; (b) loss curves of model; (c) learning rate curve of model

4.3　模型检测效果

为了验证模型检测焊缝出现根部驼峰缺陷的效果，选取激光功率为 2.5 kW，电压为 18 V，电流为 150 A，焊接速度为 1.4 m/min，引导方式为电弧引导进行验证。该焊缝前半部分有根部驼峰缺陷而后半部分为全熔透，选取连续焊缝中 9150 个样本作为测试集，输入到训练好的模型中，计算模型检测根部驼峰缺陷的准确率。图 9 为测试集中 9150 个样本对应的焊接实物与该焊缝根部驼峰缺陷检测结果的对比图。该焊缝的焊接方向为从左至右，最左边的虚线为测试集样本选取的起点，最右边的虚线为测试集样本选取的终点，中间点划线为有根部驼峰缺陷区域和全熔透区域的分界线，两条虚线之间包含 9150 个测试集样本。检测结果中 1 表示样本含有驼峰缺陷，0 表示样本为全熔透状态。当 t 为 0～3604.5 ms 时，样本检测结果为含有根部驼峰缺陷。当 t 为 2750～2900 ms 时出现误检。误检原因是该位置接近有根部驼峰缺陷区域和全熔透区域的分界线，此时熔池尾部形状有从“V”形向“U”形过渡的倾向。当 t 为 3950～4100 ms 时，检测结果在 0 和 1 之间交替变换，出现误检的原因是该区域的焊缝背部出现微弱的驼峰，如图 9 中局部放大图所示。

该模型在不同测试集样本下的检测准确性数据如表 1 所示。在有根部驼峰缺陷的测试样本中，准确率达到 95.6%。在全熔透的测试样本中，准确率达到 91.4%。在整条焊缝 9150 个测试样本中，准确率达到 94.7%，检测速度达到 25 frame/s。试验结果表明，该

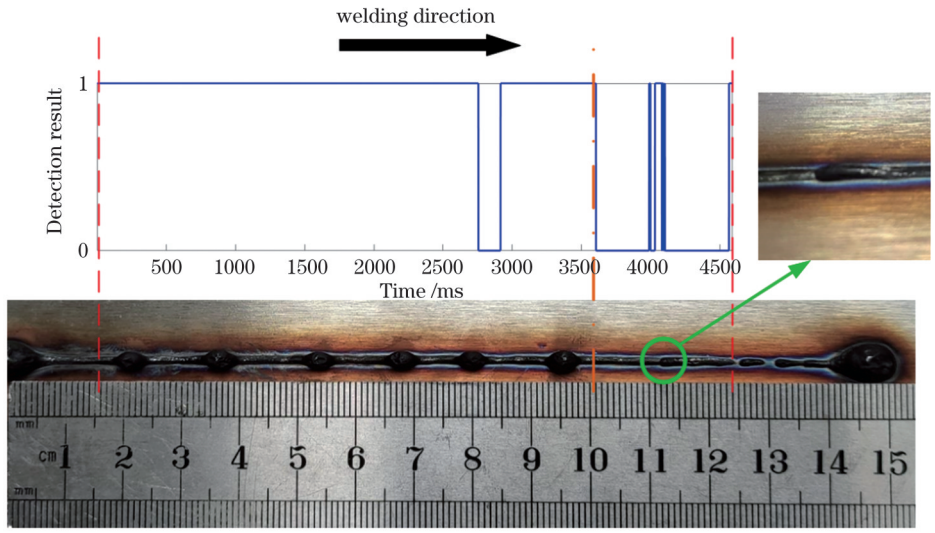

图 9　根部驼峰检测结果和真实结果对比图

Fig. 9　Comparison of detection and real results of root hump

表 1 不同测试样本下模型的检测准确性

Table 1 Detection accuracies of model under different test samples

Sample	Number of testing samples	Number of correct testing samples	Accuracy
Root hump sample	7209	6890	95.6%
Full penetration sample	1941	1775	91.4%
Sum	9150	8665	94.7%

模型能够有效检测出焊接过程中的根部驼峰缺陷。

5 结 论

利用高速摄像机采集了激光-MIG复合焊熔池的正面图像，通过对熔池图像进行处理和分析，提出一种根部焊瘤的在线检测方法。

采用基于Retinex理论的MSR增强方法处理熔池图像，可以减少熔池两侧光照不均产生的灰度差。对MSR预处理的图像进行阈值分割和形态学处理可以获取较为完整的熔池尾部图像。

通过对比焊接特征及其所处焊接状态，发现相比于全熔透样本，有根部驼峰缺陷样本的四组归一化不变矩均值至少增加了90%，而其中位数至少增加了150%，且特征值的分散程度更高。

建立的改进动态调整学习率算法的一维卷积神经网络模型，对根部驼峰缺陷具有良好的在线检测能力。对根部驼峰缺陷检测的准确率达到94.7%，可准确检测焊接过程中出现的凝固驼峰缺陷。

参 考 文 献

[1] Ma C Y, Chen B, Tan C W, et al. Characteristics of droplet transfer, molten pool formation, and weld bead formation of oscillating laser hot-wire tungsten inert gas hybrid welding[J]. Journal of Laser Applications, 2021, 33(1): 012027.

[2] 陈实现, 刘双宇, 张宏, 等. 激光-电弧复合焊等离子体特性与焊缝熔深相关性研究[J]. 兵工学报, 2017, 38(5): 978-985.
Chen S X, Liu S Y, Zhang H, et al. Study on correlation between plasma property and weld penetration in laser-arc hybrid welding [J]. Acta Armamentarii, 2017, 38(5): 978-985.

[3] 叶广文, 刘倩雯, 范西岸, 等. 激光-MIG复合焊接熔滴过渡对焊缝表面成形的影响[J]. 中国激光, 2022, 49(8): 0802012.
Ye G W, Liu Q W, Fan X A, et al. Effect of droplet transition on weld surface formation of laser-MIG hybrid welding[J]. Chinese Journal of Lasers, 2022, 49(8): 0802012.

[4] 周建, 邵晨东, 崔海超, 等. 激光-电弧复合焊在坡口中的等离子体耦合行为[J]. 中国激光, 2022, 49(2): 0202006.
Zhou J, Shao C D, Cui H C, et al. Plasma coupling behavior of laser-arc hybrid welding in groove[J]. Chinese Journal of Lasers, 2022, 49(2): 0202006.

[5] Frostevarg J. Factors affecting weld root morphology in laser keyhole welding[J]. Optics and Lasers in Engineering, 2018, 101: 89-98.

[6] Qi Y, Chen G Y, Deng S L, et al. Periodic root humps in thick-plate laser welding using steady electromagnetic force[J]. Journal of Materials Processing Technology, 2019, 273: 116247.

[7] 邹德敏, 齐锦刚, 赵琳, 等. 焊接速度对激光-电弧复合焊接焊缝成形和低温冲击韧性的影响[J]. 中国激光, 2022, 49(8): 0802014.
Zou D M, Qi J G, Zhao L, et al. Effect of welding speed on bead appearance and low-temperature impact toughness in laser-arc hybrid welding[J]. Chinese Journal of Lasers, 2022, 49(8): 0802014.

[8] Zhang H Q, Jiang M, Chen X, et al. Investigation of weld root defects in high-power full-penetration laser welding of high-strength steel[J]. Materials, 2022, 15(3): 1095.

[9] Powell J, Ilar T, Frostevarg J, et al. Weld root instabilities in fiber laser welding[J]. Journal of Laser Applications, 2015, 27(S2): S29008.

[10] Zhang R L, Tang X H, Xu L D, et al. Study of molten pool dynamics and porosity formation mechanism in full penetration fiber laser welding of Al-alloy[J]. International Journal of Heat and Mass Transfer, 2020, 148: 119089.

[11] Zhang M J, Liu T T, Hu R Z, et al. Understanding root humping in high-power laser welding of stainless steels: a combination approach[J]. The International Journal of Advanced Manufacturing Technology, 2020, 106(11): 5353-5364.

[12] Wang L, Gao X D, Kong F R. Keyhole dynamic status and spatter behavior during welding of stainless steel with adjustable-ring mode laser beam[J]. Journal of Manufacturing Processes, 2022, 74: 201-219.

[13] Gao X D, Ding D, Bai T X, et al. Weld-pool image centroid algorithm for seam-tracking vision model in arc-welding process[J]. IET Image Processing, 2011, 5(5): 410-419.

[14] Chen J Q, Wang T, Gao X D, et al. Real-time monitoring of high-power disk laser welding based on support vector machine[J]. Computers in Industry, 2018, 94: 75-81.

[15] Wang T, Gao X D, Seiji K, et al. Study of dynamic features of surface plasma in high-power disk laser welding[J]. Plasma Science and Technology, 2012, 14(3): 245-251.

[16] Fan X A, Gao X D, Huang Y H, et al. Online detection of keyhole status in a laser-MIG hybrid welding process[J]. Metals, 2022, 12(9): 1446.

[17] Gao X D, Zhang Y X. Monitoring of welding status by molten pool morphology during high-power disk laser welding[J]. Optik, 2015, 126(19): 1797-1802.

[18] Fan X A, Gao X D, Zhang N F, et al. Monitoring of 304 austenitic stainless-steel laser-MIG hybrid welding process based on EMD-SVM[J]. Journal of Manufacturing Processes, 2022, 73: 736-747.

[19] Feng Y Z, Gao X D, Zhang Y X, et al. Simulation and experiment for dynamics of laser welding keyhole and molten pool at different penetration status[J]. The International Journal of Advanced Manufacturing Technology, 2021, 112(7): 2301-2312.

[20] Zhang Y X, Han S W, Cheon J, et al. Effect of joint gap on bead formation in laser butt welding of stainless steel[J]. Journal of Materials Processing Technology, 2017, 249: 274-284.

[21] 陈根余, 夏海龙, 周聪, 等. 高功率光纤激光焊接底部驼峰的机理研究[J]. 中国激光, 2015, 42(2): 0203004.
Chen G Y, Xia H L, Zhou C, et al. Study on the mechanism of root humping of laser welding with high power fiber laser[J]. Chinese Journal of Lasers, 2015, 42(2): 0203004.

[22] Gao X D, Mo L, You D Y, et al. Tight butt joint weld detection based on optical flow and particle filtering of magneto-optical imaging[J]. Mechanical Systems and Signal Processing, 2017, 96: 16-30.

[23] 牟琦, 魏妍妍, 李姣, 等. 改进的Retinex低照度图像增强算法研究[J]. 哈尔滨工程大学学报, 2018, 39(12): 2001-2010.
Mu Q, Wei Y Y, Li J, et al. Improved Retinex low illumination image enhancement algorithm research[J]. Journal of Harbin

Engineering University, 2018, 39(12): 2001-2010.
[24] 卢志茂, 刘钦堂, 范冬梅, 等. 基于亮度划分MSR的视觉图像增强[J]. 华中科技大学学报(自然科学版), 2011, 39(S2): 99-102.
Lu Z M, Liu Q T, Fan D M, et al. Visual image enhancement based on the MSR with luminance division[J]. Journal of Huazhong University of Science and Technology (Natural Science Edition), 2011, 39(S2): 99-102.
[25] Wang M, Chen W Y, Li X D. Hand gesture recognition using valley circle feature and Hu's moments technique for robot movement control[J]. Measurement, 2016, 94: 734-744.
[26] 张子健, 马吉恩, 李旭峰, 等. 基于深度学习与Hu不变矩的绝缘子故障检测[J]. 铁道学报, 2021, 43(2): 71-77.
Zhang Z J, Ma J E, Li X F, et al. Insulator fault detection based on deep learning and Hu invariant moments[J]. Journal of the China Railway Society, 2021, 43(2): 71-77.
[27] Shamsuddin S M, Sulaiman M N, Darus M. Invarianceness of higher order centralised scaled-invariants undergo basic transformations[J]. International Journal of Computer Mathematics, 2002, 79(1): 39-48.
[28] 宫文峰, 王元哲, 陈辉, 等. 基于深度学习的无人驾驶汽车导航传感器异常诊断方法[J]. 机械工程学报, 2021, 57(24): 268-278.
Gong W F, Wang Y Z, Chen H, et al. Anomaly diagnosis for navigation sensors of unmanned autonomous vehicles based on deep learning[J]. Journal of Mechanical Engineering, 2021, 57(24): 268-278.
[29] 喻后聃, 米秋实, 赵栋, 等. 基于一维卷积神经网络的光纤周界入侵模式识别[J]. 光子学报, 2021, 50(9): 0906003.
Yu H D, Mi Q S, Zhao D, et al. Optical fiber perimeter intrusion pattern recognition based on 1D-CNN[J]. Acta Photonica Sinica, 2021, 50(9): 0906003.

Online Detection of Root Hump in Laser-MIG Hybrid Welding Based on Invariable Moment Characteristics of Molten Pool Image

Huang Yuhui, Fan Xi'an, Zhang Yanxi, Gao Xiangdong*

Guangdong Provincial Welding Engineering Technology Research Center, Guangdong University of Technology, Guangzhou 510006, *Guangdong, China*

Abstract

Objective As a reliable technology for material joint processing, laser-MIG hybrid welding (MIG welding, melt inert-gas welding) has been applied to various fields of the product manufacturing industry for decades. Due to its characteristics such as deep penetration, high welding speed, and high-quality shaping, laser-MIG hybrid welding has become the research focus. However, all kinds of defects troubling many scholars often occur in laser-MIG hybrid welding, and root hump is one of the common defects. Unlike instantaneous defects such as undercut and non-penetration, root hump defects are caused by the accumulation of molten metal flowing to the end of the pool over a a period of time. During the formation of the root hump, the weld quality is continuously affected by it. When the molten metal has solidified to form a hump, the new molten metal will continue to accumulate in the next position to form a new hump, resulting in the periodic occurrence of the root hump within a certain range. This study presents an online detection of root hump based on invariable moment characteristics of the tail molten pool, which can detect accurately root hump defect in the strong noise environment of laser-MIG hybrid welding. We hope that our innovative approach could provide the basis for the online detection of defects in laser-MIG hybrid welding.

Methods The laser-MIG hybrid welding process detection system is established by a high-speed camera, six-axis robot, arc welding machine, high-power fiber laser, and image processing computer. During laser-MIG hybrid welding, the images of the molten pool outlines are collected by the high-speed camera. To reduce the gray difference between the two sides of the molten pool when the arc is retracted or released, the multi-scale Retinex (MSR) enhancement method based on Retinex theory is used. After threshold segmentation and morphological processing, the binary images of the tail molten pool are obtained. Whereafter, the four kinds of invariant moments of the tail molten pool images are calculated. For suppressing the interference of local noise caused by random error on the tail molten pool invariant moments, the moving average method is adopted to reduce the influence of noise. The one-dimensional convolution neural network model using the improved dynamic learning rate algorithm is established, and the moving average values of the four normalized invariant moments from the tail molten pool images are used as input. The model is successful to realize the online detection of hump defects at the root of the weldment based on images of the weldment surface during laser-MIG hybrid welding.

Results and Discussions According to the comparison of the moving average values of the four normalized invariant moments from the tail molten pool images between root hump and full penetration samples, the moving average values of root hump samples are higher than those of full penetration samples. The values of the root hump are almost higher than the specific moving average value, and the full penetration is lower than it (Fig. 5). The occurrence of the root hump defect in the welding process can be preliminarily judged by the moving average values of the invariant moment. To accurately detect the root hump defects in the laser-MIG hybrid welding process, the one-dimensional convolution neural network model using the improved dynamic learning rate algorithm is established. The best accuracy of training set from training samples is 99.73%, and the best accuracy of the validation set from training samples even reaches 99.88% (Fig. 8). A continuous weld bead, whose the first half of the weld bead has root hump and the second half is normal, is used to verify the reliability of the model. The samples are detected as root hump defect samples in

the first 3604.5 ms. The false detection occurs in 2750–2900 ms. The reason for false detection is that this position is close to the boundary between the root hump area and no defect area. At this time, the moving average values of invariant moment decrease. In the latter part, the detection result alternates between 0 and 1 in 3950–4100 ms (Fig. 9). A weak hump on the back of the weld bead leads to this false detection. Although the model has some detection errors, it can still accurately detect most root hump defects with 94.7% accuracy (Table 2).

Conclusions This study adopts invariable moment characteristics of the tail molten pool to detect root hump in laser-MIG hybrid welding. Aiming at the problem of uneven illumination on both sides of the molten pool, the MSR enhancement method based on Retinex theory is adopted to reduce the gray difference on both sides of the molten pool. The moving average values of the four normalized invariant moments from the tail molten pool images coming from the image process can be used to judge the occurrence of the root hump defects. It is observed that the moving average values of the root hump samples are higher than those of the full penetration samples. A one-dimensional convolution neural network model with an improved dynamic adjusting learning rate algorithm is established to detect the root hump defects. The experimental result shows that the accuracies of the training set and the verification set can reach 99.73% and 99.88% respectively. The model is applied to detect root hump defects in continuous weld bead, whose accuracy reaches 94.7%. The root hump defects in laser-MIG hybrid welding are detected accurately, which provids a new idea for the realization of welding status and welding quality detection in laser-MIG hybrid welding.

Key words laser technique; neural network; laser-MIG hybrid welding; root hump; image of molten pool; invariant moment of image